

## Supplemental Information

### Crystallization Kinetics of Amorphous Calcium Carbonate in Confinement

Jack Cavanaugh, Michael L. Whittaker and Derk Joester

#### Contents

Materials and Methods.....	1
Supporting Figures .....	5
Supporting Movies .....	8
Table of Crystallization Events .....	9
Supporting Discussion .....	10
Finite-element analysis of gas diffusion.....	10
Supersaturation in droplets .....	14
Time delay between crystal nucleation and detection.....	15
Hypothesis testing and maximum likelihood estimate.....	16
Monte Carlo Simulation .....	18
MATLAB code for the Monte Carlo Simulation.....	19
Supporting References.....	20

#### Materials and Methods

##### Consumables

All aqueous solutions were prepared with ultra-pure water ( $\rho = 18.2 \text{ M}\Omega \text{ cm}$ ) dispensed by a Barnstead NanoDiamond UF + UV purification unit. Reagent grade (>99%)  $\text{CaCl}_2 \cdot 2\text{H}_2\text{O}$ ;  $\text{CaCO}_3$ ; calcein (>93%, Sigma-Aldrich, St. Louis, MO);  $(\text{NH}_4)_2\text{CO}_3$  (ca. 30%  $\text{NH}_3$ , Alpha Aesar, Haverhill, MA); and rhodamine B (MP Biomedicals) were used without further purification. The fluorosilicone oil was HFE7500 (Novec™ Engineered Fluid, 3M™, St. Paul, MN) with 2 wt% of a perfluoropolyether-polyethyleneglycol block-copolymer (PFPE-PEG-PFPE) surfactant (008-FluoroSurfactant, RAN Biotechnologies, Beverly, MA). Device fabrication used soda-lime glass masks (Nanofilm, Valley View, OH); SU8 2035 photoresist (MicroChem, Newton, MA); 3-inch polished ( $\langle 110 \rangle \pm 0.5^\circ$ ) NP silicon wafers (International Wafer Service, Colfax, CA); polydimethylsiloxane (PDMS) and crosslinker (Sylgard 184 Silicone Elastomer, Dow Corning, Midland, MI); glass coverslips (36x60 mm, No. 1-1/2 thickness, Ted Pella, Redding, CA); trichloro(1H,1H,2H,2H-perfluorooctyl) silane (Sigma-Aldrich, St. Louis, MO); polytetrafluoroethylene (PTFE, ID: 0.3 mm, OD: 0.76 mm) and Tygon® (ID: 0.64 mm, OD: 2.46 mm) tubing (Cole-Parmer, Vernon Hills, IL).

##### Synthesis of bulk ACC standard

Calcium carbonate (ACC) was synthesized by rapid mixing of a cold aqueous solution of 1 M  $\text{CaCl}_2$  (50 mL, pH 5.6) with a cold aqueous solution of 1 M  $\text{Na}_2\text{CO}_3$  (50 mL, pH 11.7). Solutions were stored on ice for 2 h. Solutions were mixed

by vigorous shaking for 30 s. The resulting white precipitate was immediately collected by vacuum filtration through a 100-mm diameter Whatman no. 4 cellulose filter paper, washed 3 times with 5 mL cool water ( $T = 10\text{ }^{\circ}\text{C}$ ), and then dried under vacuum (R.T.,  $P \approx 10\text{ Pa} = 10^{-1}\text{ Torr}$ , 24 h). Characterization was performed immediately thereafter.

### Device Fabrication

All microfluidic devices were produced through soft lithography of PDMS.<sup>1</sup> Device masters were fabricated by photolithography of SU8 positive photoresist on silicon wafers. Similar procedures were used for both drop makers and storage devices.

Flow-focusing droplet maker devices required a single layer of SU8, while the droplet storage devices required a two-layer process. Soda-lime glass masks were fabricated with a maskless writer ( $\mu\text{PG501}$ , Heidelberg Instruments, Heidelberg, DE) using designs generated in AutoCAD (Autodesk, Inc.). Following the manufacturer's protocol, SU8 was spin-coated onto wafers at 2250 rpm and baked for 2 min at  $65\text{ }^{\circ}\text{C}$  and then 8 min at  $95\text{ }^{\circ}\text{C}$  to produce a uniform and dry coating  $\sim 50\text{ }\mu\text{m}$  in thickness. SU8 was exposed to UV (160 mJ) in a mask aligner (MABA6, Süss MicroTec, Garching, DE) and baked for 2 min at  $65\text{ }^{\circ}\text{C}$  and then 6 min at  $95\text{ }^{\circ}\text{C}$  to crosslink the design geometry.

For those masters where a second layer was required, wafers were allowed to cool for 2 min following the post-exposure bake of the first layer. The second layer was then applied by spin-coating under similar conditions. To prepare the master for alignment to a second mask, alignment marks in four corners of the design were revealed by selectively dissolving unexposed SU8. Selective dissolution in the region of the alignment marks was carried out by pipetting sufficient propylene glycol monomethyl ether acetate (PGMEA) to cover the marks, waiting  $\sim 2\text{ min}$ , and then removing the PGMEA solution by flowing compressed air in the direction away from the device design. This process was repeated as necessary until contrast between the Si wafer and alignment marks was apparent. The second SU8 coating was then exposed with the second mask.

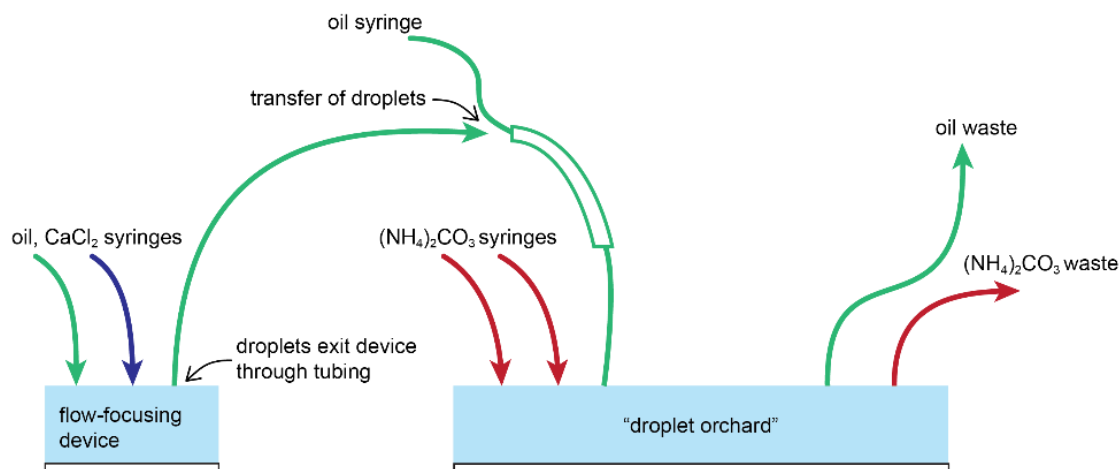
Following exposure of all SU8 layers, the unexposed SU8 was dissolved using PGMEA and dried with filtered compressed air. A one-time surface treatment was completed by placing masters into a desiccator equilibrated with trichloro(1H,1H,2H,2H-perfluorooctyl) silane for 2 h to facilitate demolding of PDMS in subsequent castings.

A mixture of 10:1 PDMS and crosslinker was mixed thoroughly, degassed at 50 Torr in a desiccator to remove air bubbles, and cast onto masters. The PDMS was cured at  $130\text{ }^{\circ}\text{C}$  for 10 min on a hotplate. After curing, inlet and outlet holes were punched in the PDMS with a blunt 19-gauge syringe needle and the PDMS was bonded to a glass coverslip ( $36\times 60\text{ mm}$ , No. 1-1/2 thickness, Ted Pella, Redding, CA) by treating both surfaces with air plasma (Harrick Plasma, Ithaca, NY) at  $7\times 10^{-1}\text{ mbar}$  pressure. A surface treatment was applied to devices by placing them in a desiccator equilibrated with trichloro(1H,1H,2H,2H-perfluorooctyl) silane for 2 h to promote wetting of the fluorinated oil to the channel surfaces and repel aqueous droplets.

### Device Operation

The droplet storage device was prepared by attaching  $\sim 5\text{ cm}$  lengths of PTFE tubing to the inlets and outlets of the droplet storage channel and the aqueous  $(\text{NH}_4)_2\text{CO}_3$  delivery channels (**Scheme S1**). The PTFE tubing was terminated with  $\sim 2\text{ cm}$  lengths of Tygon<sup>®</sup> tubing to serve as flexible connectors to additional PTFE tubing. The droplet storage channel was connected via additional PTFE tubing to a Hamilton glass 1 mL syringe loaded with fluorinated oil, and the syringe was compressed to fill the tubing and droplet storage channel completely with oil. The device was flushed with fluorinated oil for at least 1 minute.

Droplets were produced using a flow-focusing geometry with a nozzle width of  $50\text{ }\mu\text{m}$ . Aqueous 1 M  $\text{CaCl}_2$  (pH 5.6) and fluorinated oil were loaded into separate 1 mL glass Hamilton syringes attached via PTFE tubing to the inlets of the device. Fluid flow was controlled using separate syringe pumps (KDS 200, KD Scientific, Holliston, MA). Flow rates of approximately  $300\text{ }\mu\text{L/hr}$  for the oil phase and  $200\text{ }\mu\text{L/hr}$  for the aqueous phase produced  $\sim 100\text{ }\mu\text{m}$  diameter droplets.



**Scheme S1.** Schematic of the device setup. Separate microfluidic chips were used for droplet generation and droplet storage. Colored lines represent tubing which transport fluoros oil (green), aqueous 1 M  $\text{CaCl}_2$  (blue), and aqueous 1.5 M  $(\text{NH}_4)_2\text{CO}_3$  (red). The outlet tubing of the droplet-generating device was briefly connected to the inlet tubing of the droplet storage device to transfer droplets.

Droplets were directed to the inlet tubing of the droplet storage device by detaching the oil syringe line at the Tygon® connector, with care taken to ensure that air bubbles were not introduced during the exchange of tubing. In the connector, a plug of droplets accumulated which was visible by naked eye. After the plug of droplets was  $\sim 2$  cm long, containing  $\sim 10^4$  droplets, the droplet maker chip was detached, and the oil syringe was reattached, taking care again to ensure that air bubbles were not introduced. To load droplets from the inlet tubing into the droplet storage channel, the device was inverted (glass coverslip faced upward) and placed  $\sim 20$  cm above the height of the oil syringe for  $\sim 5$ – $10$  min so that droplets were driven into the channel by buoyancy in the oil ( $\rho = 1.61$  g/mL). The loaded droplet storage device was returned to the upright position. Before initiating precipitation, excess droplets were allowed time to flow out of the storage channel.

### Precipitation

Two Hamilton glass 5 mL syringes were loaded with 1.5 M  $(\text{NH}_4)_2\text{CO}_3$  (pH 8.8) and attached to the two aqueous  $(\text{NH}_4)_2\text{CO}_3$  delivery channels of the droplet storage device. Flow rate was set at 200  $\mu\text{L/hr}$  for both channels. The beginning of an experiment was recorded as the time that solution filled the aqueous  $(\text{NH}_4)_2\text{CO}_3$  delivery channels. Waste  $(\text{NH}_4)_2\text{CO}_3$  was directed out of the device through PTFE tubing and collected for disposal. Approximately every 24 h, the syringes were loaded with fresh 1.5 M  $(\text{NH}_4)_2\text{CO}_3$  to continue the supply to the droplets.

### Imaging

The droplet storage device was mounted to a Leica DMI6000b inverted microscope and imaged under crossed-polarizers with 100 ms camera exposure. Images were automatically acquired every 5 min at 9 different stage locations with a Märzhäuser automated stage controlled using MetaMorph Imaging software.

### Confocal Raman spectroscopy

Raman spectra were recorded using a Horiba LabRAM HR Evolution confocal Raman microscope. A 532-nm excitation laser (49 mW) was focused through the cover glass on the bottom of the device and into a single droplet. All spectra (including powder standards) were recorded using a 50x objective (0.75 numerical aperture), 1-3 second acquisition time with 20–50 accumulations, 1800 gratings/mm, and 100- $\mu\text{m}$  confocal pinhole. While many spectra were acquired from 0-3000  $\text{cm}^{-1}$ , some spectra from mineral in droplets were acquired from 600-1200  $\text{cm}^{-1}$  for expediency. To mount the storage device to the upright microscope, the device was inverted by flipping carefully along the axis of the droplet storage channel to reduce the chance of dislodging droplets from wells.

For spectra acquired at early times, a device was loaded with droplets as described above, i.e. by inverting the device. Spectra from the initial stages of mineralization were acquired ~30 min after initiating flow of aqueous  $(\text{NH}_4)_2\text{CO}_3$  (1.5 M) into the flanking delivery channels.

#### **Confocal fluorescence microscopy**

Droplets were made with 30  $\mu\text{g}/\text{mL}$  calcein and 40  $\mu\text{g}/\text{mL}$  rhodamine in addition to 1 M  $\text{CaCl}_2$ . Confocal fluorescence images of droplets were acquired before and after precipitation using a Leica DMI6000 inverted microscope equipped with Yokogawa CSU-X1 spinning disk module with Microlens-enhanced Nipkow disk. Fluorescence from calcein was excited by a 488-nm solid state laser, filtered at 525 nm, and detected with 25-ms exposure. Fluorescence from rhodamine B was excited by a 561-nm solid state laser, filtered at 600 nm, and detected with 200-ms exposure. The filter wheel disk speed was 5000 rpm. For the reconstruction of the composite color images in Figure 2D and 2E, calcein fluorescence intensity was rendered in green and rhodamine fluorescence intensity was rendered in red. Note that calcein segregates to the ACC precipitate, and rhodamine segregates to the PDMS.

## Supporting Figures

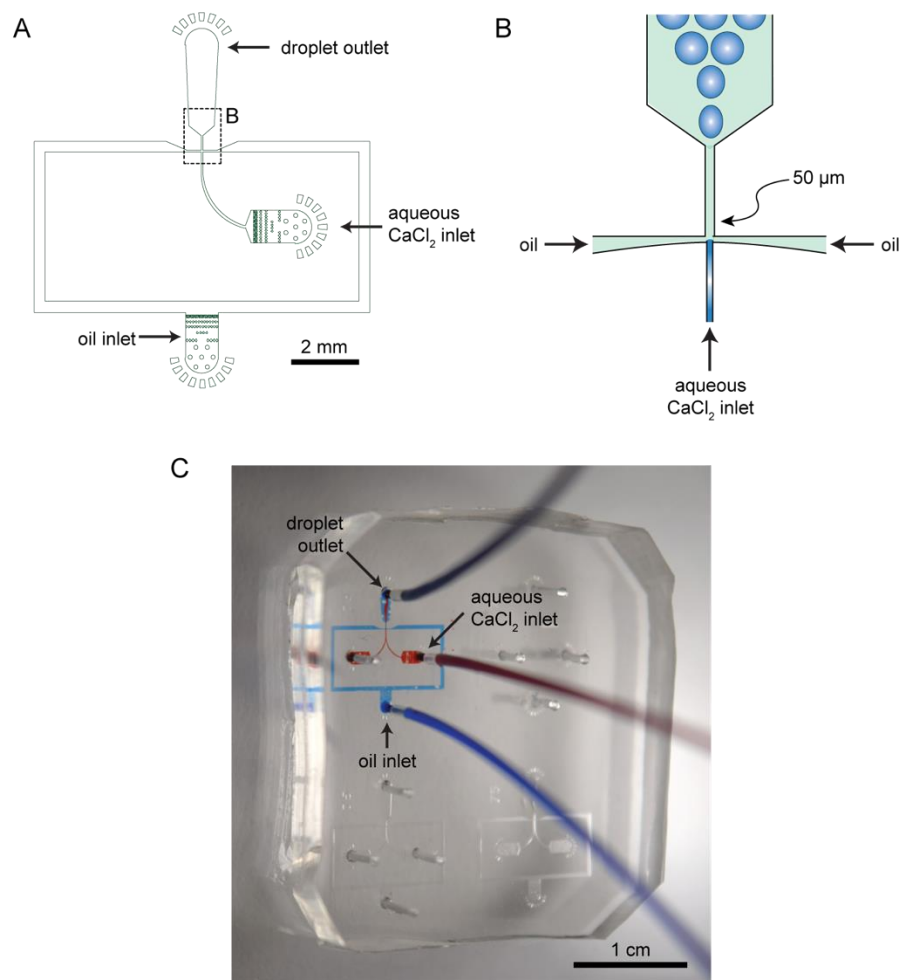


**Figure S1.** (A) CAD drawing showing the 2D layout of the flow-focusing device. Height of the device is uniform and  $\sim 50 \mu\text{m}$ . (B) Schematic of the hydrodynamic flow-focusing geometry used to produce aqueous droplets in the fluorinated oil. The width of the junction where droplets form was  $50 \mu\text{m}$ . Location in (A) is denoted by the black dashed box. (C) Photograph of a flow-focusing device mounted on a glass slide. To provide color contrast in this photograph, channels were filled with two aqueous solutions dyed with red and blue food coloring. The real-world device includes an optional secondary aqueous inlet for mixing two solutions; in this study, the secondary inlet was not used. Note, the device pictured has a junction width of  $75 \mu\text{m}$  compared to the  $50 \mu\text{m}$  junction used in this study.

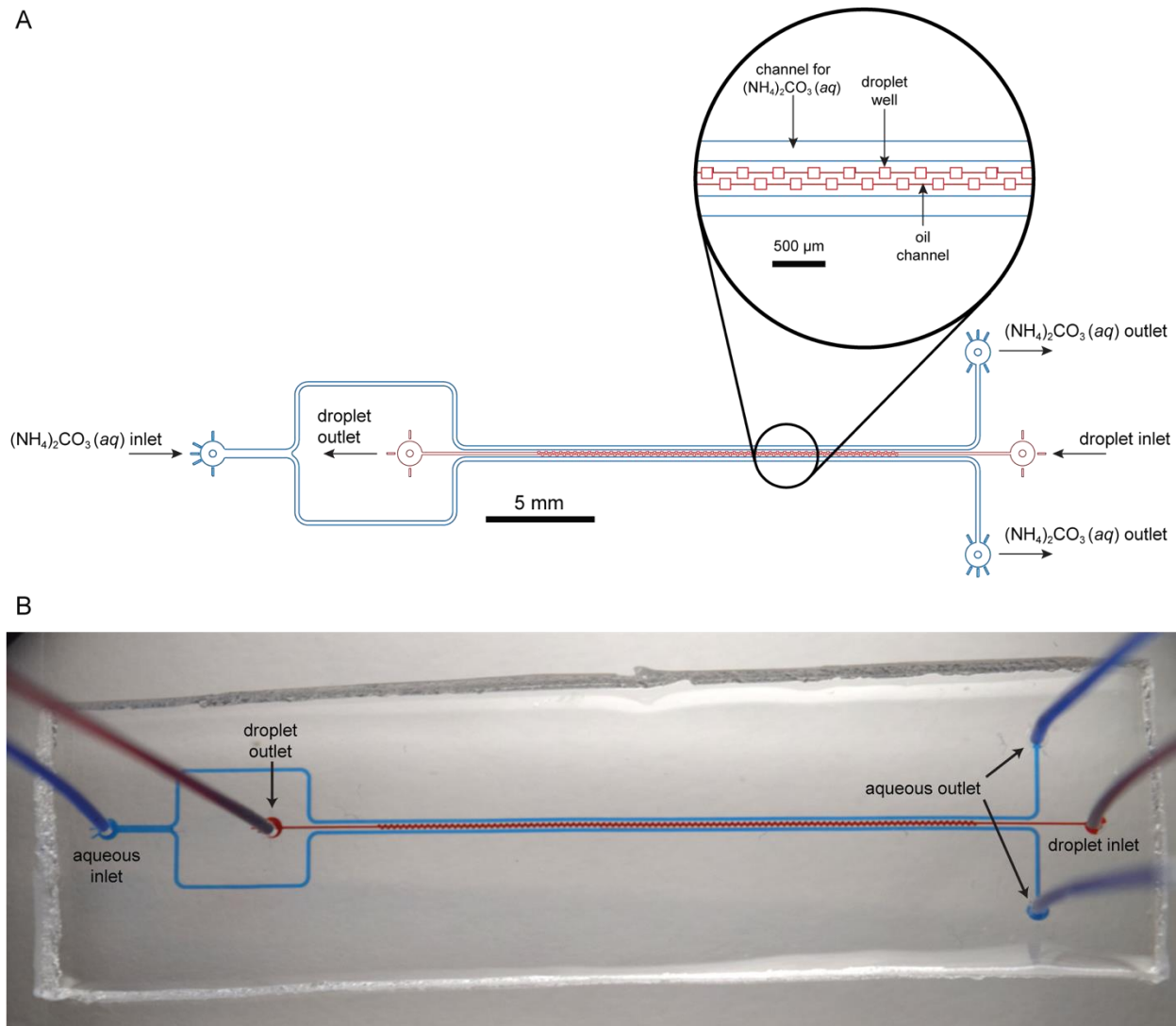


**Figure S2.** (A) CAD drawing showing the 2D layout of the droplet storage device (droplet orchard). Inset details the storage wells (light red) offset from the fluorinated oil channel for droplet delivery (red), and channels for delivery of aqueous  $(\text{NH}_4)_2\text{CO}_3$  (blue). Height of the wells is  $100\ \mu\text{m}$ , while the remaining device height is  $50\ \mu\text{m}$ . (B) Photograph of a droplet orchard device (here with 196 wells) mounted on a glass slide. To provide color contrast in this photograph, the aqueous  $(\text{NH}_4)_2\text{CO}_3$  delivery channels were charged with an aqueous solution dyed with blue food coloring. The oil/droplet delivery channel was charged with an aqueous solution of red food coloring.

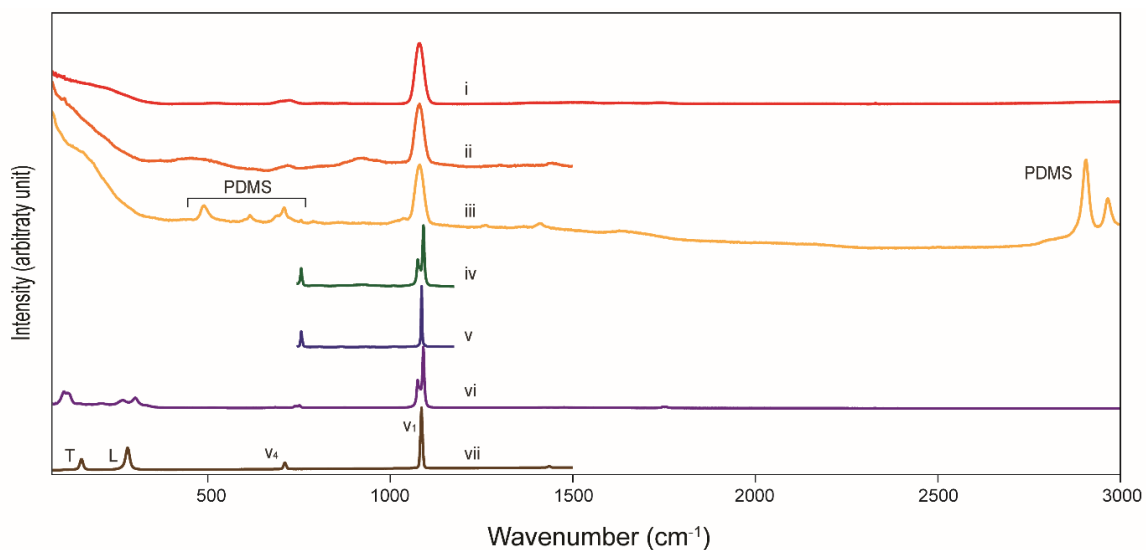


**Figure S3.** Raman spectra of (i) bulk synthetic ACC, (ii) ACC in a liposome, (iii) mineral in a droplet at  $t \approx 30$  minutes, (iv-v) mineral in two droplets after crystallization, bulk (vi) vaterite and (vii) calcite powders. Labels denote the carbonate symmetric stretching ( $v_1$ ), in-plane bending ( $v_4$ ), lattice translational (T), and lattice librational (L) modes, along with additional peaks associated with PDMS in the background. No background subtraction was applied. Spectra were normalized by the most intense carbonate  $v_1$  mode peak.

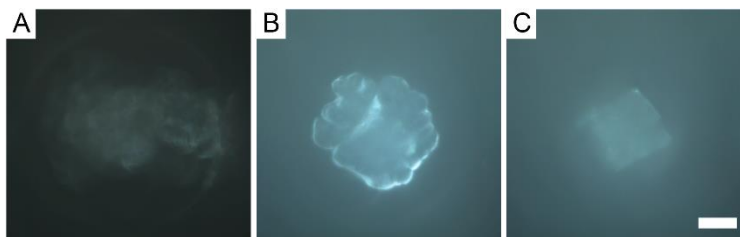


**Figure S4.** Representative reflected-light images of mineral in droplets, which were acquired alongside Raman spectra that correspond to (A) ACC, (B) vaterite, and (C) calcite. Scale bar represents 20  $\mu\text{m}$ .

## Supporting Movies

**Movie S1.** Loading the droplet orchard. Real-time video compiled from time-lapse bright field images. Aqueous droplets in fluorinated oil ( $d=100\ \mu\text{m}$ ) travel in a channel with rectangular cross section ( $w = 100\ \mu\text{m}$ ,  $h = 50\ \mu\text{m}$ ), and are therefore compressed in the view direction. On encountering a well ( $h = 100\ \mu\text{m}$ ), droplets relax to a spherical shape and are effectively trapped as long as the flow rate is on the order of  $5\ \mu\text{L}/\text{hour}$  or less. For reference of scale, please refer to the  $100\text{-}\mu\text{m}$  edge length of the wells in each image.

**Movie S2.** ACC precipitation. Time-lapse video (frame rate =  $1\ \text{s}^{-1}$ ) compiled from images captured at 5-minute intervals showing ACC precipitation after onset of  $1.5\ \text{M}\ (\text{NH}_4)_2\text{CO}_3$  flow through the delivery channels. For reference of scale, please refer to the  $100\text{-}\mu\text{m}$  edge length of the wells in each image.

**Movie S3.** Rotating polycrystal. Real-time video compiled from a series of images showing a polycrystalline vaterite precipitate rotating slowly between crossed polarizers. A) Brightness-enhanced to reveal droplet interface and walls of well. B) Brightness as recorded. Note that images were acquired at the end of an experiment and hours after the flow of  $1.5\ \text{M}\ (\text{NH}_4)_2\text{CO}_3$  had ceased; accordingly, the droplet had decreased in size and rotated more freely within the well. For reference of scale, please refer to the  $100\text{-}\mu\text{m}$  edge length of the wells in each image.

**Movie S4.** Rotating single crystal. Real-time video compiled from a series of images showing a single-crystalline calcite precipitate rotating slowly between crossed polarizers, extinguishing periodically. A) Brightness-enhanced to reveal droplet interface and walls of well. B) Brightness as recorded. Note that images were acquired at the end of an experiment and hours after the flow of  $1.5\ \text{M}\ (\text{NH}_4)_2\text{CO}_3$  had ceased; accordingly, the droplet had decreased in size and rotated more freely within the well. For reference of scale, please refer to the  $100\text{-}\mu\text{m}$  edge length of the wells in each image.

**Movie S5-7.** Droplet crystallization (a-c). Time-lapse video (frame rate =  $1\ \text{s}^{-1}$ ) showing crystal detection and growth within a droplet from each of the three experiments presented in this study. For reference of scale, please refer to the  $100\text{-}\mu\text{m}$  edge length of the wells in each image.

## Table of Crystallization Events

**Table S1.** List of the time that crystallization events were observed. Plots in Fig. 3A and B. draw on this data.

	Experiment (a)	Experiment (b)	Experiment (c)
Event	Time (min)	Time (min)	Time (min)
1	30	5	160
2	1255	85	455
3	1550	125	630
4	1750	415	690
5	2790	450	960
6	4515	620	1565
7		765	1850
8		795	2155
9		1010	2395
10		1050	3595
11		1060	4170
12		1490	4500
13		1575	4520
14		1725	4830
15		1815	4975
16		2150	5005
17		2230	5130
18		2695	5255
19		2700	5355
20		2835	5585
21		3120	
22		3630	
23			
24			
25			
26			

## Supporting Discussion

### Finite-element analysis of gas diffusion

To assess whether the time scale of gas transport might impact the measurement of a crystal nucleation rate, diffusion of gas across the microfluidic device from the aqueous delivery channel was modelled by finite-element analysis (COMSOL Multiphysics®). A 2D model was implemented as a basic approximation of the 3D device geometry. The 2D device geometry was drawn in AutoCAD and imported into COMSOL® (Figure S5), with three domains representing PDMS, the fluorinated oil, and an aqueous droplet. The geometry included a 20-nm gap, an approximate maximum length of the surfactant molecule, between the droplet and the PDMS to avoid a short circuit for diffusion. Other values for the gap were tested, as discussed later in this section.

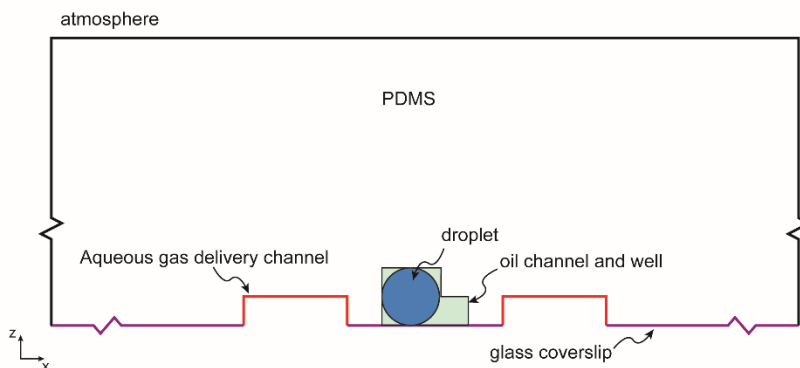


**Figure S5.** Schematic of the 2D geometry used to model gas diffusion in the microfluidic device by finite-element analysis. Three domains include the PDMS (white), fluorinated oil channel and well (green), and droplet (blue). Additional materials represented by boundaries include the aqueous gas delivery channels (red), glass coverslip (purple), and atmosphere (black).

Gas diffusion was modelled with the built-in equations for “transport of dilute species,” which can integrate the diffusion equation:

$$\frac{\partial c}{\partial t} - D \cdot \nabla^2 c = 0 \quad (\text{S1})$$

where,  $c$  is the concentration and  $D$  is the diffusivity of the dilute species. To implement discontinuities in  $c$  and  $D$  at the interface between materials, a separate set of variables were integrated for each domain and the concentrations were summed in a global variable. Boundary conditions and domain properties for gas diffusion are determined by the solubility limit and diffusivity of the gas in each material.<sup>2</sup> At an interface between two materials, the internal boundary condition is given by the system of equations:

$$\frac{c_1}{S_1} = \frac{c_2}{S_2} \quad (\text{S2})$$

$$D_1 \nabla c_1 = D_2 \nabla c_2 \quad (\text{S3})$$

where  $S$  is the solubility of the gas in each material, as distinguished by subscripts. Equation S2 implements a partition coefficient, where the concentration is discontinuous across the interface between the materials because of a difference in solubility. The equation results from Henry's law and the continuity of partial pressure across material interfaces.<sup>2</sup> Equation S3 implements continuous mass flux of the gas across the interface.

The weak-formulation of partial differential equations, which is implemented by finite element analysis, relaxes the continuity requirements for derivatives of  $c$ . Accordingly, the equality in Equation S3 is not applied in the model for the boundary condition between two materials. However, continuity of  $c$  itself is a requirement for integration,<sup>3</sup> which impedes realistic modelling of gas concentration profiles because a discontinuity is expected between material interfaces. To force a discontinuity in concentration, a "penalty" or "stiff-spring" method is usually applied.<sup>4</sup> Therefore, we applied a point-wise constraint at the boundary between domains with the following expression:

$$c_2 - S_2/S_1 \cdot c_1 \quad (S4)$$

Diffusivity and solubility parameters were either identified in literature or calculated from basic assumptions and validated by testing whether results vary if the parameter differed by an order of magnitude (**Table S2**).

**Table S2.** Diffusivity and solubility of CO<sub>2</sub> and NH<sub>3</sub> in the three simulation domains

Material domain	CO <sub>2</sub>		NH <sub>3</sub>	
	D (cm <sup>2</sup> /s)	S (mM/atm)	D (cm <sup>2</sup> /s)	S (mM/atm)
PDMS	8.7×10 <sup>-6</sup> (a)	94.8 (b)	4.2×10 <sup>-6</sup> (a)	487 (a)
HFE7500 (no mixing)	11×10 <sup>-6</sup> (c)	138.9 (e)	14×10 <sup>-6</sup> (c)	100 (f)
HFE7500 (perfect mixing)	1×10 <sup>3</sup> (d)	138.9 (e)	1×10 <sup>3</sup> (d)	100 (f)
Droplet	1×10 <sup>3</sup> (d)	1×10 <sup>9</sup> (d)	1×10 <sup>3</sup> (d)	1×10 <sup>9</sup> (d)

(a) from ref. 5

(b) from ref. 6

(c) Estimated by the Stokes-Einstein relation

(d) Non-physical value entered to approximate an idealized behavior (perfect mixing, no mixing, or perfect sink)

(e) Manufacturer's information provided upon request.

(f) Order of magnitude estimation. The solution was negligibly impacted for values from 0.2 to 5 times the estimate.

The droplet was treated as a perfect sink for gas in the concentration regimes and pH of interest, as nearly all CO<sub>2</sub> is expected to precipitate as CaCO<sub>3</sub> after supersaturation is established and before a solubility limit is reached. A perfect sink was implemented simply by setting the solubility and diffusivity of gasses in the droplet domain to several orders of magnitude higher than the concentration regimes and transport rates of interest to the study.

Parameters for the fluorinated oil were assumed to be negligibly impacted by the 2 wt% content of the fluorinated surfactant. Diffusivity of gas in the fluorinated oil was not available in literature or from the manufacturer. For an upper bound on the delivery of gas to droplets, perfect mixing of the oil was assumed. An assumption of perfect mixing is also supported by the frequent rotation of droplets within wells over the course of experiments, due to small perturbances in pressure. For a lower bound, purely diffusive transport (no mixing) was assumed and the diffusivity was estimated using the Stokes-Einstein relation:

$$D = \frac{T k_B}{6\pi \eta r} \quad (S5)$$

The Stokes-Einstein relation estimates the diffusivity due to Brownian motion of a spherical particle in a low Reynolds number fluid. Particle radius,  $r$ , was approximated by half the kinematic diameter of each gaseous species.<sup>5</sup> The dynamic viscosity of the fluid,  $\eta$ , is calculated from the kinematic viscosity,  $\nu$ , and the density,  $\rho$ , by the equation  $\eta = \nu \cdot \rho$ . Per the manufacturer's information,  $\nu = 0.77 \text{ mm}^2/\text{s}$  and  $\rho = 1.6 \text{ g/mL}$  for HFE7500. At room temperature, we estimate the diffusivity of  $\text{CO}_2$  and  $\text{NH}_3$  in HFE7500 as shown in **Table S3**.

**Table S3.** Diffusivity of gasses in HFE7500 as estimated by the Stokes-Einstein relation

Gas species	Kinematic diameter (pm)	D (cm <sup>2</sup> /s)
Carbon dioxide	165 (a)	$11 \times 10^{-6}$
Ammonia	130 (a)	$14 \times 10^{-6}$

(a) from ref. 5

Initial concentration of the gasses in PDMS and fluorinated oil were calculated by Henry's law, assuming equilibrium with atmosphere. Boundary conditions are summarized in **Table S4**. The lower external boundary with the glass coverslip for all materials was fixed as an impermeable barrier. The boundary condition between PDMS and atmosphere was fixed using Henry's law. Gas concentration at the boundary with the source channel was also fixed by Henry's law, where partial pressures in aqueous solution were calculated for equilibrium speciation using MINTEQ software ( $p_{\text{CO}_2} = 0.038 \text{ atm}$ ,  $p_{\text{NH}_3} = 0.019 \text{ atm}$ ). Constant partial pressure in aqueous solution was assumed because the fluid in the entire channel is expected to be replaced every 2.5 seconds for the flow rate used in experiments (200  $\mu\text{L/hr}$ , or 6 mm/s).

At the PDMS-oil and oil-droplet interfaces, a discontinuity in gas concentration results from a difference in solubility. The discontinuities were implemented by the "penalty" method using a "point-wise constraint", as discussed above. The importance of applying a "penalty" between the PDMS and HFE7500 is reduced by similarity in diffusivity and solubility of each gas in the two materials.

**Table S4.** Internal and external boundary conditions for the three simulation domains

Boundary	Type	Equation
PDMS – Source channel	Dirichlet	$c_{\text{src}} = p_{\text{aq}} \cdot S_{\text{PDMS}}$
PDMS – Fluorinated oil	Point-wise constraint	$c_{\text{oil}} - S_{\text{oil}}/S_{\text{PDMS}} \cdot c_{\text{PDMS}}$
PDMS – Air	Dirichlet	$c_{\text{atm}} = p_{\text{atm}} \cdot S_{\text{PDMS}}$
Fluorinated Oil – Droplet	Point-wise constraint	$c_{\text{drp}} - S_{\text{drp}}/S_{\text{oil}} \cdot c_{\text{oil}}$
All domains – Glass coverslip	Neumann	$\frac{\partial c}{\partial y} = 0$

Mesh properties were finalized after conducting tests for convergence of the solution (**Table S5**). Convergence was evaluated with respect to the time elapsed before two events of interest: (1) supersaturation with respect to ACC and (2) molar equivalency of  $\text{Ca}^{2+}$  and  $\text{CO}_3^{2-}$ . The "resolution of narrow regions" for the mesh was identified as the most sensitive parameter in terms of effect on the solution and computation time (**Figure S6A**). The solution was said to have converged for an integer increase in the mesh resolution which produced a difference of less than 0.1 seconds for the time of events (1) and (2) compared to the previous solution.

A range of values were also tested for the gap between the droplet and PDMS. In real-world experiments, no wetting was observed between the droplet and the device surface—which, again, was surface-treated with a highly fluorinated molecule. Accordingly, a nonzero gap between the droplet and device surface was chosen for the model geometry.

**Table S5.** Parameters tested to refine the finite-element model.

Parameter	Tested values	Value selected from test
Mesh: “resolution of narrow regions”	1 – 20	7
Gap between droplet and PDMS	1000 – 10 nm	20 nm

This model predicted that, in the “slow” case of entirely diffusive transport, the supersaturation with respect to ACC is established within 500 milliseconds (**Figure S6C**). Assuming fast equilibration and precipitation in the droplets, the model further indicates that delivery of stoichiometric amounts of  $\text{CO}_2$  and  $\text{NH}_3$  for the precipitation of all  $\text{Ca}^{2+}$  as  $\text{CaCO}_3$  takes less than 30 minutes. In the real-world “droplet orchard” experiments, growth of the ACC phase became negligibly slow after 30 minutes, indicating that the phase was in metastable equilibrium. Also, >99% of crystals were detected hours to days after the initiation of  $(\text{NH}_4)_2\text{CO}_3$  flow. Therefore, the finite element model supports the assumption that gas delivery is not a limiting factor in the precipitation of ACC and does not strongly influence the supersaturation of crystalline  $\text{CaCO}_3$  over the timespan of experiments.

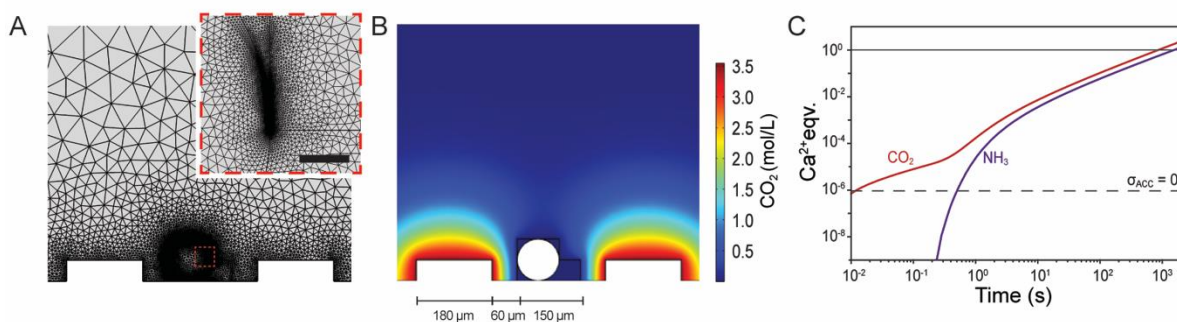


**Figure S6.** (A) Finite-element mesh imposed over the device geometry where the “resolution of narrow regions” was set to 7. Inset (red dashed box) scale bar represents  $10\ \mu\text{m}$ . (B) Map of  $\text{CO}_2$  concentration for the region of interest at 10 s, showing the gradient in concentration from the two aqueous delivery channels to the droplet. (C) Plot of stoichiometric equivalents of  $\text{CO}_2$  and  $\text{NH}_3$  delivered to the droplet versus time  $t$ . Using the highest ACC solubility reported in literature ( $\text{p}K_{\text{sp}} = 6.04$ ), droplets are predicted to be supersaturated for ACC above the dashed horizontal line.

The presented model is strictly limited as a basic check on our assumptions. Given the limitations of available data for the diffusion and solubility of gasses, we have not yet increased the complexity of the model to include 3D geometry and rates of dissolution (i.e. a reaction-diffusion model). Given the experimental observations of ACC precipitation and growth, we speculate that such additions to the model are unlikely to decrease the gas transport rate sufficiently to alter conclusions.

## Supersaturation in droplets

Slowed growth of the ACC phase after ~30 minutes suggests that supersaturation with respect to ACC reduced to nearly zero. Under these conditions, particles may still increase in size through coarsening, but the total volume of ACC remains constant. In comparison, over 99% of crystals were detected hours to days after initiation of  $(\text{NH}_4)_2\text{CO}_3$  flow. Therefore, ACC was likely near metastable equilibrium with the encapsulated solution at the time of crystal nucleation. At equilibrium ( $\sigma_{\text{ACC}} = 0$ ), the concentration of  $\text{Ca}^{2+}$  and  $\text{CO}_3^{2-}$  in solution is given by the solubility product:

$$K_{\text{sp,ACC}} = [\text{Ca}^{2+}][\text{CO}_3^{2-}] \quad (\text{S6})$$

$$\sigma_{\text{CaCO}_3} = \ln\left(\frac{[\text{Ca}^{2+}][\text{CO}_3^{2-}]}{K_{\text{sp,CaCO}_3}}\right) = \ln\left(\frac{K_{\text{sp,ACC}}}{K_{\text{sp,CaCO}_3}}\right) \quad (\text{S7})$$

The solubility product of ACC in droplets is not known, and multiple ACC solubility products are reported in literature. For literature values (**Table S6**), we calculated the supersaturation with respect to vaterite ( $K_{\text{sp,v}} = 0.012 \text{ mM}^2$ ), aragonite ( $K_{\text{sp,a}} = 0.0046 \text{ mM}^2$ ), and calcite ( $K_{\text{sp,c}} = 0.0033 \text{ mM}^2$ ) at  $T = 25 \text{ }^\circ\text{C}$ .<sup>7</sup>

**Table S6.** Supersaturation with respect to vaterite, aragonite, and calcite for ACC solubility products in literature.

$K_{\text{sp,ACC}} \text{ (mM}^2\text{)}$	$\sigma$ vaterite	$\sigma$ aragonite	$\sigma$ calcite
0.031 <sup>(a)</sup>	0.93	1.9	2.2
0.038 <sup>(a)</sup>	1.1	2.1	2.4
0.41 <sup>(b)</sup>	3.5	4.5	4.8
0.91 <sup>(c)</sup>	4.3	5.3	5.6

(a) from ref. 8; (b) from ref. 9; (c) from ref. 10.

## Time delay between crystal nucleation and detection

This study relies on detection of a crystal with optical microscopy to approximate the time of nucleation. Birefringent particles were typically 1-10  $\mu\text{m}$  wide in images at detection, or three orders of magnitude larger than the theoretical diameter of a crystal nucleus.<sup>11</sup> Validity of the time-to-detection approximation for time of nucleation was evaluated by estimating the delay between crystal nucleation and detection.

Lacking information about the particles prior to detection, we sought an order of magnitude estimate for the time-to-detection. The growth rate of three particles was measured in proxy by the brightness detected in sequential images under polarized light microscopy, i.e. by a 2D projection of the birefringent material. A brightness threshold was applied to the image sequences in NIH ImageJ to determine particle area. For convenience, time  $t = 0$  at first detection for each particle.

A general power law was fit to the  $A$  versus  $t$  dataset (**Figure S7**). Note, the model choice is merely phenomenological, i.e. it is not derived from a known or theoretical growth mechanism. It is, nonetheless, useful for extrapolating the observed growth rate to early times to estimate the average time-to-detection,  $t_0$ .

$$A(t) = a \cdot (t + t_0)^b \quad (\text{S8})$$

Equation S8 was fit to the dataset using the MATLAB curve fitting tool, and the estimated time-to-detection was  $t_0 = 44$  seconds ( $a = 6.9 \times 10^{-4}$ ,  $b = 1.9$ ,  $R^2 = 0.90$ ). Accordingly, we estimate the delay between nucleation and detection to be on the order of minutes. In comparison, crystals were detected on the scale of hours to days after ACC precipitation. In other words, the available evidence suggests that the growth rate is sufficiently fast to approximate the time of crystal nucleation from the time of detection.

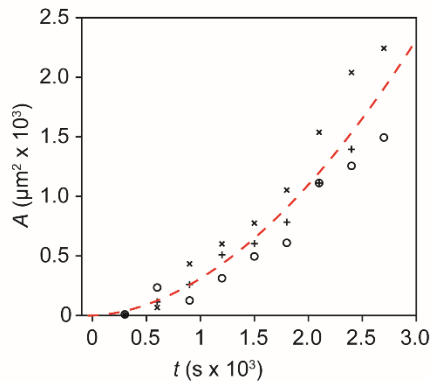


**Figure S7.** Projected Area,  $A$ , versus time,  $t$ , for growth of three different birefringent precipitate2 (open circles, "+", and "x") and a general power law fit to the data points (red dashed line).

## Hypothesis testing and maximum likelihood estimate

This study presents data from three independent crystallization experiments conducted using “droplet orchard” devices. The datasets generated by droplet nucleation experiments include only one experimental variable: the time-of-detection  $t$  of a crystal. Nucleation events occur randomly, but when a large sample of independent droplets are observed over time, the dataset becomes representative of the overall probability distribution of nucleation events and an average rate can be calculated.

A hypothesis test was conducted to judge whether the three datasets come from the same probability distribution. In other words, we would like to determine whether it is justifiable to combine the three datasets and analyze them in aggregate. We applied an analogue to the 2-sample Kolmogorov-Smirnov test for comparing two samples: the  $k$ -sample Anderson-Darling test,<sup>12</sup> which can test whether three datasets come from the same unspecified continuous probability distribution. In this case, we define the null hypothesis to be that the three sets of observations were drawn from the same distribution. The  $k$ -sample test has previously been implemented in MATLAB,<sup>13</sup> and so this script was simply applied to the “droplet orchard” datasets. A significance level of  $\alpha = 0.01$  was chosen in consideration of the noise that could be expected in the dataset given the high sensitivity of nucleation to impurities and sources of potential energy like mechanical vibrations. For the calculated probability value  $p = 0.013$ , the 3-sample Anderson-Darling test failed to reject the null hypothesis that the three sets of observations were drawn from the same distribution. We therefore chose to aggregate the datasets and model the experiments with a single nucleation rate.

As discussed in the main body of text, for an experiment in which nucleation events occur continuously and independently at a constant average nucleation rate, nucleation theory predicts that the univariate dataset is drawn from an exponential distribution as shown in Equation 3. Accordingly, an additional hypothesis test was conducted to judge whether it is justifiable to model the aggregated dataset with an exponential distribution. We applied the 1-sample Anderson-Darling test for exponentially distributed data,<sup>14</sup> which is a built-in function in the “Statistics and Machine Learning” toolbox for MATLAB (“adtest”). The 1-sample Anderson-Darling test failed to reject the null hypothesis ( $\alpha = 0.010$ ;  $p = 0.211$ ) that the aggregated data come from an exponential distribution. This conclusion means that we lack evidence that would recommend against modelling the aggregated data using an exponential distribution; however, it does not rule out the possibility that a more complex model might better explain the dataset.

An exponential distribution was fit to the univariate data using maximum-likelihood estimation (MLE) for the rate parameter, or the mean of the distribution. Crystallization was observed in just 16% of all droplets before experiments were terminated. Note that the three experiments from which data was used in this analysis were terminated at different times. For droplets in which crystallization was not observed by the time the experiment was terminated, the latest time point was recorded as a right-censored observation. While the exact time of crystallization is unknown for such right-censored observations, the censored data point records a lower bound which is incorporated into the MLE. An exponential distribution was fit to the dataset of exact and censored observations using a function that is included in the “Statistics and Machine Learning” toolbox for MATLAB (“expfit”). MLE for the rate parameter of the exponential distribution from which the data are sampled predicted that  $J = 1.2 \text{ cm}^{-3} \text{ s}^{-1}$  with a 99% confidence interval from  $0.8 \text{ cm}^{-3} \text{ s}^{-1}$  to  $1.7 \text{ cm}^{-3} \text{ s}^{-1}$ .

Of the 48 crystals detected in these experiments, 6 (12.5%) appeared faceted in the first image frame following detection (5 minutes later). In the above, we assumed that vaterite nucleated first and very quickly converted to calcite. Under the alternate assumption that calcite nucleated directly (i.e. without a vaterite intermediate), the MLE for the nucleation rate of vaterite was recalculated. To do so, we right-censored the time-of-detection for the 6 droplets where calcite was observed (Figure S8A). This means that the droplet was removed from the experiment at that time. However, the information that no vaterite nucleated prior to removal is factored into the MLE. Under this assumption, MLE predicted that  $J_{\text{vat}} = 1.1 \text{ cm}^{-3} \text{ s}^{-1}$  with a 99% confidence interval from  $0.7$  to  $1.5 \text{ cm}^{-3} \text{ s}^{-1}$  and  $J_{\text{calcite}} = 0.15 \text{ cm}^{-3} \text{ s}^{-1}$  with a 99% confidence interval from  $0.04 \text{ cm}^{-3} \text{ s}^{-1}$  to  $0.36 \text{ cm}^{-3} \text{ s}^{-1}$ .

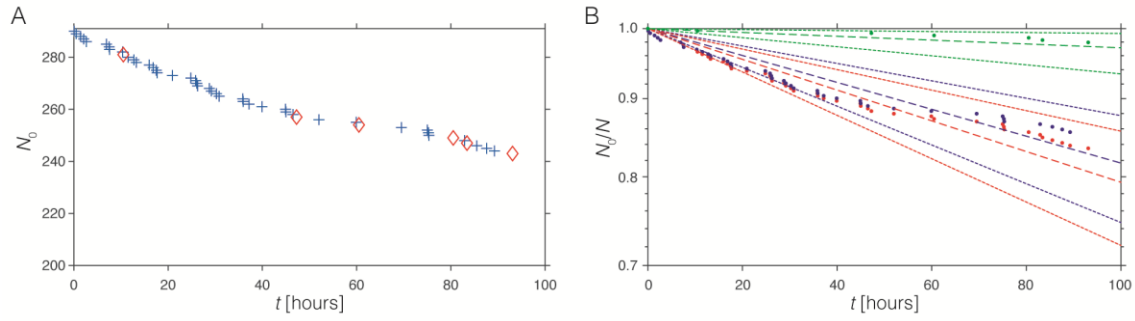


**Figure S8.** A) The number of droplets without crystals,  $N_0$ , as a function of time. Nucleation events resulting in droplets with vaterite precipitates are indicated by "+". Events resulting in calcite crystals with no indication of vaterite formation are indicated by red diamonds. B) Plot of  $N_0/N$  vs. time assuming all nucleation events lead to vaterite (red circles), with MLE fit (red dashed line), and 99% confidence intervals (red dotted lines); assuming that only events marked with blue "+" in (A) lead to vaterite (blue circles, MLE fit blue dashed line, CI blue dotted lines) and that events marked with red diamonds in (A) lead to calcite (green circles, MLE fit green dashed line, CI green dotted lines).

## Monte Carlo Simulation

Monte Carlo simulations were performed in MATLAB. Crystallization in each droplet was treated as a random process, with the probability that crystallization did not occur at each time step  $\Delta t$  equal to  $P_0(\Delta t)$ . The probability  $P_0(\Delta t)$  was calculated from Equation 1 for  $J = 1.23 \text{ cm}^{-3} \text{ s}^{-1}$ , the nucleation rate predicted from the droplet orchard experiments. Droplet volume  $V = 523.6 \text{ pL}$  was calculated for spherical droplets with  $100\text{-}\mu\text{m}$  diameter. A time step  $\Delta t = 1 \text{ h}$  was sufficient to resolve the curvature of the exponential failure distribution over 100 h experiments. For these parameters,  $P_0(\Delta t) = 0.9977$  for each droplet. Experiments were performed with 97 droplets, the average number of droplets from the three droplet orchard experiments.

The simulation code (included the following section) performed the follow procedure. For each time step, Monte Carlo steps were evaluated for the cut-off value given by  $P_0(\Delta t)$ . For each droplet that did not contain a crystal, a pseudorandom number  $n$ ;  $0 < n < 1$  was generated to determine whether a crystal did ( $n > P_0(\Delta t)$ ) or did not ( $n \leq P_0(\Delta t)$ ) nucleate. The number of droplets which remained in the amorphous state was calculated and recorded for use in the subsequent time step. Following all time steps, the fraction of droplets that did not contain a crystal,  $N_0/N$ , was calculated for all times.

At any given time step, the Monte Carlo simulation is equivalent to a binomial experiment where the number of trials is equal to the number of droplets which remain in the amorphous state. The binomial distribution approaches symmetry for a large number of trials and a small probability of success. The  $N_0/N$  results of  $10^5$  experiments were plotted on a histogram for each time to confirm the symmetrical shape and relationship to the binomial distribution (**Figure S9**). For  $t \geq 20$  hours, the distribution of experiments is approximately symmetrical. At times earlier than 20 hours and approaching  $t = 0$ , the distribution becomes less symmetrical for two reasons: (1) as an artefact of discretization into bins and (2) as a consequence of the finite sample of droplets in each experiment.

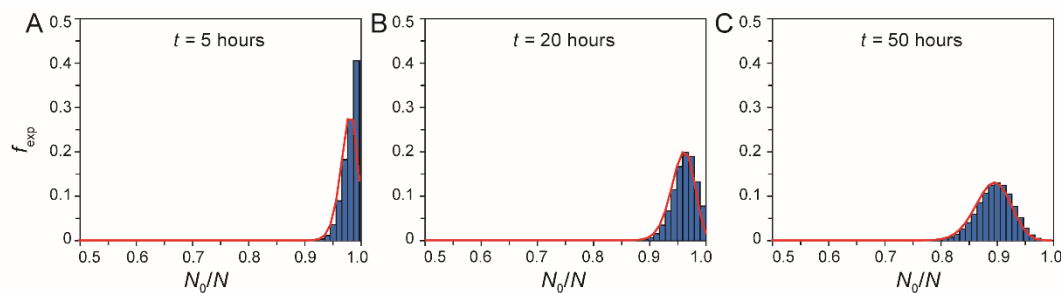


**Figure S9.** Histogram showing the fraction  $f_{\text{exp}}$  of  $10^5$  Monte Carlo experiments with a given  $N_0/N$  result at  $t = 5, 20,$  and  $50$  hours and probability density function (red line) of the binomial distribution with mean equal to the rate parameter of the Monte Carlo experiments.

Given the approximately symmetric distribution of  $N_0/N$ , the data for all experiments were binned into 68/95/99.7% symmetric quantiles centered at the mean ( $P_0(\Delta t)$ ) of each time step. A convergence test was performed to determine the number of experiments  $E$  required to calculate quantiles for all theoretical experiments accurate to a difference of one droplet, or  $N_0/N = 0.0116$  (**Table S7**). It was determined that  $10^5$  experiments were sufficient to determine quantiles.

**Table S7.** Maximum absolute difference between all 68/95/99.7% quantiles of  $N_0/N$  v.  $t$  for simulations with  $E_1$  and  $E_2$  experiments, respectively.

$E_1 / E_2$	Maximum absolute difference
$10^2 / 10^3$	0.0233
$10^3 / 10^4$	0.0174
$10^4 / 10^5$	0.0116
$10^5 / 10^6$	0.0116

## MATLAB code for the Monte Carlo Simulation

```
%% Simulation settings
experiments = 10^5; % total number of individual MC experiments
duration = 100; % total time of experiments in hours
attempts = duration; % time resolution of crystallization events
time = 0:duration/attempts:duration; % hours
N = 97; % Initial number of droplets with only solid phase being ACC
d = 100*10^-4; % diameter of individual droplet in cm
V = 4/3*pi*(d/2)^3; % droplet volume in cm^3
J = 1.23; % cm^-3 s^-1, Nucleation rate from linear fit to 297-droplet
experiment

%% Monte Carlo Simulation
P0t = exp(-J*V*time*3600); % Probability that a droplet does not contain a
crystal
cutoff = P0t(2); % Probability that a droplet has crystallized in one time
step

% Initialize containers for experiment results
crystals = zeros(experiments, attempts + 1);

% Loop for each experiment
parfor experiment = 1:experiments

    droplets = N; % Experiment begins with N0 ACC-droplets

    % Monte Carlo steps for each experiment:
    for step = 2:(attempts + 1)

        % Test ACC-droplets for crystallization
        crystals(experiment, step) = sum(rand(droplets, 1) > cutoff);

        % Calculate remaining ACC-droplets after step
        droplets = droplets - crystals(experiment, step);
    end
end

N0 = N - cumsum(crystals,2); % Count ACC-droplets for all times
f_ACC = N0/N; % Calculate fraction ACC-droplets for all times

bins = 0.5*[1 - 0.997 1 - 0.95 1 - 0.68 1 1 + 0.68 1 + 0.95 1 + 0.997];
envelopes = quantile(f_ACC, bins, 1); % Bin experiments into 68/95/99.7%
quantiles
```

## Supporting References

- 1 D. C. Duffy, J. C. McDonald, O. J. A. Schueller, G. M. Whitesides, *Anal. Chem.*, 1998, **70**, 4974-4984.
- 2 M.-C. Kim, R. H. W. Lam, T. Thorsen, H. H. Asada, *Microfluid. Nanofluid.*, 2013, **15**, 285-296.
- 3 J. Wendt, *Computational Fluid Dynamics: An Introduction*, 3 ed., Springer-Verlag, Berlin Heidelberg, 2009.
- 4 I. M. Smith, D. V. Griffiths, L. Margetts, *Programming the Finite Element Method*, John Wiley & Sons, 2013.
- 5 C. Makhloufi, D. Roizard, E. Favre, *J. Membr. Sci.*, 2013, **441**, 63-72.
- 6 T. C. Merkel, V. I. Bondar, K. Nagai, B. D. Freeman, I. Pinnau, *J. Polym. Sci., Part B: Polym. Phys.*, 2000, **38**, 415-434.
- 7 L. N. Plummer, E. Busenberg, *Geochim. Cosmochim. Acta*, 1982, **46**, 30.
- 8 D. Gebauer, A. Völkel, H. Cölfen, *Science*, 2008, **322**, 1819-1822.
- 9 L. Brečević, A. E. Nielsen, *J. Cryst. Growth*, 1989, **98**, 504-510.
- 10 J. R. Clarkson, T. J. Price, C. J. Adams, *J. Chem. Soc., Faraday Trans.*, 1992, **88**, 243-249.
- 11 A. Navrotsky, *Proc. Natl. Acad. Sci. USA*, 2004, **101**, 12096-12101.
- 12 F. W. Scholz, M. A. Stephens, *J. Am. Stat. Assoc.*, 1987, **82**, 918-924.
- 13 A. Trujillo-Ortiz, 2008.
- 14 M. A. Stephens, *Goodness-of-fit Techniques*, 1986, **68**, 97-193.